Supplementary Materials

1 Supplementary Movies

- **Movie 1** shows the all-atom simulation 8BARs-AA (see Fig. 2 of the main text).
- **Movie 2** shows the first 50 ns from one of the shape-based coarse-grained (SBCG) simulations 8BARs-CG, i.e., the time period over which the membrane bending proceeds to approximately the same extent as in simulation 8BARs-AA (see Fig. 2 of the main text).
- **Movie 3** shows complete tubulation observed in the SBCG simulation 43BARs-3 (see Fig. 3A of the main text).
- **Movie 4** shows complete tubulation observed in the SBCG simulation 24BARs-3 (see Fig. 3B of the main text).

2 Supplementary Methods

Parameterization procedures have been explained in previous publications (Arkhipov et al., 2006b,a; Freddolino et al., 2008; Arkhipov et al., 2008). The specific SBCG model for the N-BAR domain interacting with a membrane, used here, is taken without modifications from Arkhipov et al. (2008). Below, we briefly summarize the procedures relevant for the parameterization of the SBCG force-field. See Arkhipov et al. (2008) for details.

2.1 SBCG force-field parametrization for proteins

The terms for bonded interaction are described by $V_{bond}(r) = K_b(r - r_0)^2$ and $V_{angle}(\theta) = K_{angle}(\theta - \theta_0)^2$ for bond length r and angle θ, where K_{bond}, r_0, K_{angle}, θ_0 are the force-field parameters. These parameters for the SBCG protein model are tuned to match the observables from an all-atom MD simulation of a single N-BAR domain dimer. For this purpose, one follows for each CG bond and angle the distances between the centers of mass of corresponding atomic domains; CG parameters are chosen so that in the CG simulation of a protein unit, the mean distances (angles) and respective root mean square deviations (RMSD) agree with those found in the all-atom simulation (Arkhipov et al., 2008).

For the nonbonded interactions, LJ radius σ_{mn} for a pair of CG beads m and n is computed as $\sigma_{mn} = (\sigma_m + \sigma_n)/2$, where σ_m is the LJ radius of the mth bead. σ_m for the mth CG bead is calculated as the radius of gyration of its all-atom domain, increased by 2 Å. The increase is done to account for the size of atoms on the surface of the domain; 2 Å is approximately an average LJ radius of an atom in the CHARMM force field. The LJ interaction strength ϵ_{mn} for the pair of beads m and n is computed as $\epsilon_{nm} = \sqrt{\epsilon_m \epsilon_m}$, where ϵ_m and ϵ_n are the strengths for each bead. The value of ϵ_m was assigned for each bead m based on the hydrophobic solvent accessible surface area (SASA) for the all-atom domain represented by the bead,

$$\epsilon_m = \epsilon_{max} \left(\frac{SASA_m^{hphob}}{SASA_m^{tot}} \right)^2 , \tag{1}$$

where $SASA_m^{hphob}$ and $SASA_m^{tot}$ are the hydrophobic and total SASA of the domain m, and $\epsilon_{max} = 10$ kcal/mol (Arkhipov et al., 2008). Note that such a choice leads to a simple description of the hydrophobic/hydrophilic partition in solution, as the latter is modeled implicitly. Indeed, for a pair of CG beads that both represent pieces of protein with only hydrophilic residues on the surface, the ratio in Eq. 1 is zero, leading to $\epsilon_{ij} = 0$. In such case the two beads are free to dissociate in "solution". For two completely hydrophobic beads we choose $\epsilon_{mn} = 10$ kcal/mol, which is significantly higher than the thermal energy ($k_B T \approx 0.6$ kcal/mol at $T = 300$ K), resulting in strong attraction between two such beads. This choice

of the LJ parameters has been justified by comparisons of SBCG and all-atom simulations for a single N-BAR domain dimer on a membrane patch (Arkhipov et al., 2008).

2.2 SBCG force-field parametrization for lipid membrane

Interactions for SBCG beads representing the lipid membrane are parameterized based on all-atom simulations of a DOPC membrane patch. The length of the bond r_0 between the head and tail SBCG beads, and the bond strength K_b, are tuned to reproduce the average membrane leaflet thickness, as well as its RMSD, obtained in the all-atom simulation (Arkhipov et al., 2008). The values used are $r_0 = 12\,\text{Å}$ and $K_b = 0.2\,\text{kcal/(Å}^2\text{mol)}$.

The LJ parameters for lipid beads are chosen to reproduce the area per lipid ($\sim$70 Å^2). The LJ energy ϵ_i for a tail (head) bead is 10 kcal/mol (0.1 kcal/mol); LJ radius σ_i is 6.8 Å for both.

2.3 Details of SBCG simulations

All SBCG simulations were carried out as specified earlier (Arkhipov et al., 2008) using NAMD (Phillips et al., 2005); analysis and visualization of simulation trajectories were performed using VMD (Humphrey et al., 1996). The integration time step was $\Delta t = 100\,\text{fs}$. The times reported in this study are actual simulation times (Δt times number of integration steps). A 35 Å cutoff was used for the non-bonded interactions. Periodic boundary conditions were used; the membrane was discontinuous (i.e., forming stripes; Fig. 3 of the main text shows one such stripe) in the longer dimension (rather than one continuous sheet) to allow for bending and complete tubulation (c.f. Fig. 4 of the main text). Periodic boxes for simulations of long and short membrane patches are $400\times16\times150\,\text{nm}^3$ and $100\times16\times50\,\text{nm}^3$, respectively. The simulations were run assuming constant volume and temperature, the latter being maintained at 310 K using a Langevin thermostat (Phillips et al., 2005). The membrane was a randomized mixture of neutral and negative lipids, with 30% of negative lipids. The large membrane patches for simulations with 24 or 43 N-BAR domains were composed from copies of smaller patches ($64\times16\,\text{nm}^2$), that were pre-equilibrated for 500 ns. The large membrane patches were $\sim$200 nm in length, corresponding approximately to the circumference of a tube with a radius of 30 nm. N-BAR domains were placed on the planar membranes in such a way that tips and N-terminal helices of the proteins were at the level of the head beads of the membrane, which roughly corresponds to embedding those protein parts at the level of the lipids' phosphate groups.

With the described SBCG simulations, the scaling of the performance of NAMD (Phillips et al., 2005) with an increasing number of processors for parallel runs was found to be the same as for average all-atom simulations. As an example, for the 24BARs simulations (which would require up to 60,000,000 atoms to simulate in an all-atom representation, water included), 1.3 μs were simulated in a day on 6 nodes of Abe, an Intel 64 Linux Cluster at NCSA (6 nodes corresponding to 48 cores with the frequency of 2.33 GHz each). This

performance, together with the 6,000-fold reduction in system size (150-fold for the protein and membrane, but larger overall, since the model is solvent-free), allowed us to follow the dynamics of a macromolecular assembly 200 nm in size for up to 200 μs for individual simulations.

Since the time step used is 100 fs, the direct speed up is 100$\times$ in comparison with all-atom simulations that typically use time step of 1 fs. An SBCG simulation such as 24BARs-4, $\sim$200 μs in duration and with $\sim$10,000 CG beads, required $\sim$150 days on NCSA Abe. The combined simulation time in the present study was 500 μs for short membrane patches and over 600 μs for 24BARs and 43BARs simulations, resulting in more than a millisecond of overall simulation time.

2.4 Details of the all-atom simulation

We performed an all-atom simulation of one N-BAR domain lattice on a patch of DOPC/DOPS membrane. This simulation served the purpose of comparing all-atom and SBCG approaches. A small membrane patch with 30% DOPS and 70% DOPC lipids (9.8 $\times$ 4.6 nm^2) was prepared as described in Arkhipov et al. (2008) and equlibrated for 10 ns. The equilibrated patch was duplicated and truncated, yielding a membrane patch of 64 $\times$ 8 nm^2, and was equilibrated for additional 15 ns. Eight N-BAR domains (constructed as in Arkhipov et al. (2008)) were placed onto the membrane surface with their N-terminal helices partially buried between lipid headgroups. The TIP3P water model (Jorgensen et al., 1983) was used to solvate the system and Na^+ ions were subsequently added to neutralize the net charge, resulting in a system of 2,304,973 atoms with dimensions 80$\times$8$\times$36 nm^3. Similar to the SBCG simulations, solution paddings (8 nm long) were added on both size of the long axis of the membrane to facilitate membrane bending.

To allow lipids and proteins to establish proper contacts, the system was equilibrated for 5 ns with C_α atoms of N-BAR domains being harmonically constrained to their initial positions (the constraints' spring constant was 1 kcal/(mol Å^2)), then for another 5 ns with the proteins released and the tails of lipids harmonically constrained with the same spring constant, and then for additional 10 ns with all components unconstrained. To make sure that the N-helices reach proper depth into the membrane, we used steered molecular dynamics (SMD) (Isralewitz et al., 2001) to pull the N-helices toward the hydrophobic/hydrophilic interface of the lipids. A constant force, 0.2 kcal/(mol Å), was exerted on the C_α atoms of residues 1 to 24 for 5 ns. Then the system was equilibrated for 5 ns with C_α atoms of residues 1 to 24 harmonically constrained to the positions they have reached, with the same spring constant as above, followed by another 10 ns equilibration with all constraints removed. The pre-equilibrated all-atom system was then simulated for 200 ns without any constraints (simulation 8BARs-AA).

The CHARMM (MacKerell et al., 1998; Feller, 2000) force field was used.

Periodic boundary conditions were applied, and simulations were carried out in an NpT ensemble (temperature 310 K and pressure 1 atm). A Langevin thermostat with a damping coefficient of 0.5 ps^{-1} maintained temperature; pressure was maintained via a Langevin-piston barostat with a piston period and damping time of 2 ps each. Short range non-bonded interactions were cut-off smoothly between 10 and 12 Å. The PME algorithm was used to compute long-range electrostatic interactions. The implementation of these algorithms in NAMD is described in Phillips et al. (2005). Simulations of membrane patches alone were performed with an integration time step of 1 fs; a 2 fs time step was employed in simulation 8BARs-AA. The 200 ns simulation was executed on computers at NCSA and TACC (Texas Advanced Computing Center, Austin, TX) at a speed of about 3 ns per day.

2.5 Measurement of membrane curvature, θ, and S

The membrane curvatures were computed as follows. The positions of the tail beads of the membrane were collected at a given time moment and projected onto the x, z-plane, where the x-axis is parallel to the long dimension of the membrane patch at time $t = 0$, and the z-axis is perpendicular to the plane of the patch at $t = 0$. The obtained membrane profile in the x, z-plane was fitted with the equation of a circle, using a least squares fitting method. The radius of the circle that provided the best fit to the membrane profile was used as the current radius of curvature of the membrane. No significant curvature developed in the y-dimension.

Sometimes in the simulations, the local membrane bending exhibited higher curvature than the overall global curvature computed with the method described above. However, such local features, which are transient, are not relevant for the comparison of the simulations to the tubes observed experimentally. Therefore, we report everywhere the global curvature radius computed via fitting the membrane profile to a circle.

The tube dimensions highlighted by arrows in Fig. 3 of the main text were computed as distances (within the plane perpendicular to the tube axis) between the opposing centers of bilayers that constitute the tube's walls.

The angle θ is between a row of N-BAR domains and the x-axis (which corresponds to the long dimension of the membrane patch), measured in the $x - y$ plane as shown in Fig. 1B of the main text. Each such row of N-BARs is shown in Fig. 1B in two alternating colors, either red and deep violet, or green and yellow. At each frame of the trajectory, for a given row, we selected all CG beads in that row excluding the N-helices, projected their positions on the $x - y$ plane, calculated for such coordinate selection the direction of the principal axis aligned with the long dimension of the selection, and computed θ as the angle between this axis and x-axis.

S is the distance between two adjacent rows of N-BARs, also in the $x - y$ plane (Fig. 1B of the main text). At each frame of the trajectory, for two rows, we employed a procedure similar to that for obtaining θ, which resulted

in two selections of coordinates projected on the $x - y$ plane. Principal axes of these selections, aligned with their long dimensions, were computed; these two axes pointed generally in similar directions, but were not exactly parallel due to thermal noise. The distance between the centers of the two selections in the $x - y$ plane was then projected on each of the two axes, and S was computed as the average of the two projections.

3 Supplementary Results

Control simulations

Simulations of the membrane without N-BAR domains were performed as a control (simulations "Membrane-tube", "Membrane-half-tube", and "Membrane-1", 2, and 3 in Table 1 of the main text). Simulations "Membrane-tube" and "Membrane-half-tube" were started from intermediate structures in simulation 43BARs-3 (Fig. S1). In case of simulation "Membrane-tube", all N-BAR domains were removed from 43BARs-3 after a complete tube had formed; in case of simulation "Membrane-half-tube", all N-BAR domains were removed from 43BARs-3 at 10 μs, when the membrane had been bent significantly, but the edges were not fused yet. The completely formed membrane tube without N-BAR domains remained stable over 10 μs, suggesting that the tube sculpted by the N-BAR domain lattice is a relatively stable membrane structure. In the case of simulation "Membrane-half-tube", the membrane that was bent, but not fused into a complete tube, relaxed within 10 μs to a less curved conformation (Fig. S1). One expects that given enough time this system would relax to a completely flat (on average) membrane. A membrane without N-BAR domains, starting from a planar conformation (simulations "Membrane-i", with $i = 1, 2, 3, 4$), remained in an overall flat conformation for 60 μs, except for relatively small random fluctuations (Fig. S2). Thus, the membrane curvature observed in our simulations of systems with both membrane and N-BAR domains is not an artifact of the membrane model, rather, N-BAR domains actively induce membrane curvature and drive the formation of membrane tubes.

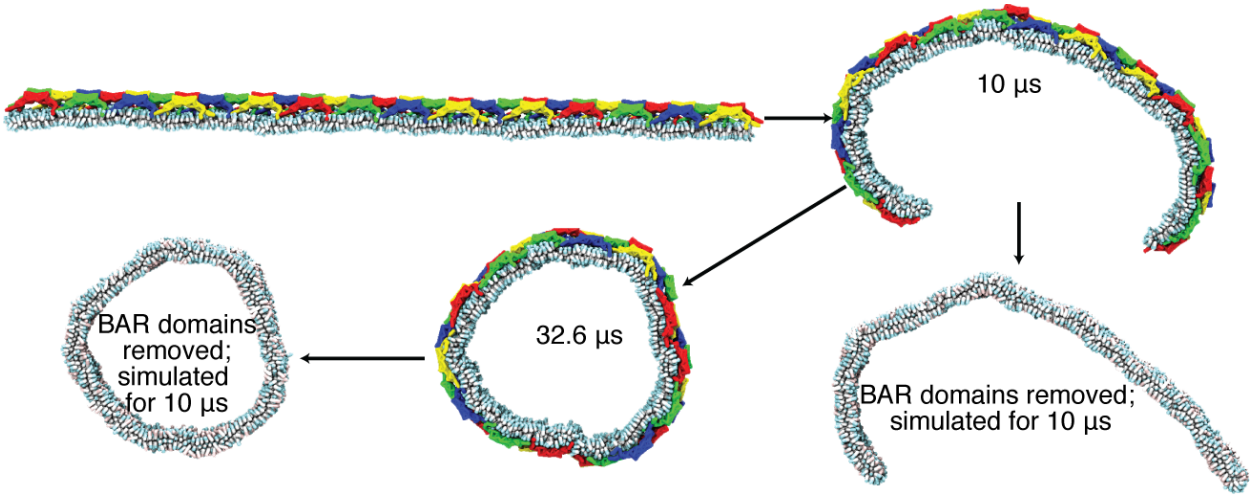

Figure S1: Stability of membrane structures (half-tube and tube) without N-BAR domains. The snapshots of the tubulation process by N-BAR domains are taken from simulation 43BARs-3. At times 10 μs and 33 μs, when the membrane forms a half-tubular and a tubular structure, N-BAR domains were removed. Both N-BAR domain-free membrane structures were simulated for 10 μs.

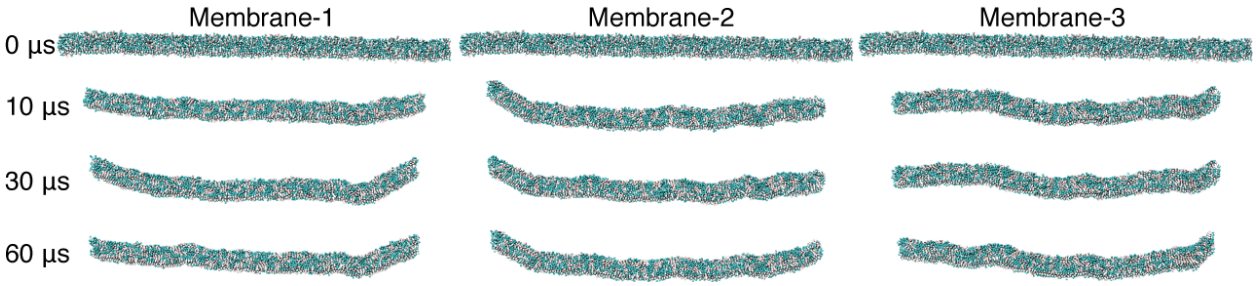

Figure S2: Simulations of a lipid membrane without N-BAR domains. The membrane used here is the same as that in simulations 24BARs. Side views of the membrane in three independent simulations at time 0, 10, 30 and 60 μs.

Flexibility of N-BAR domain dimers

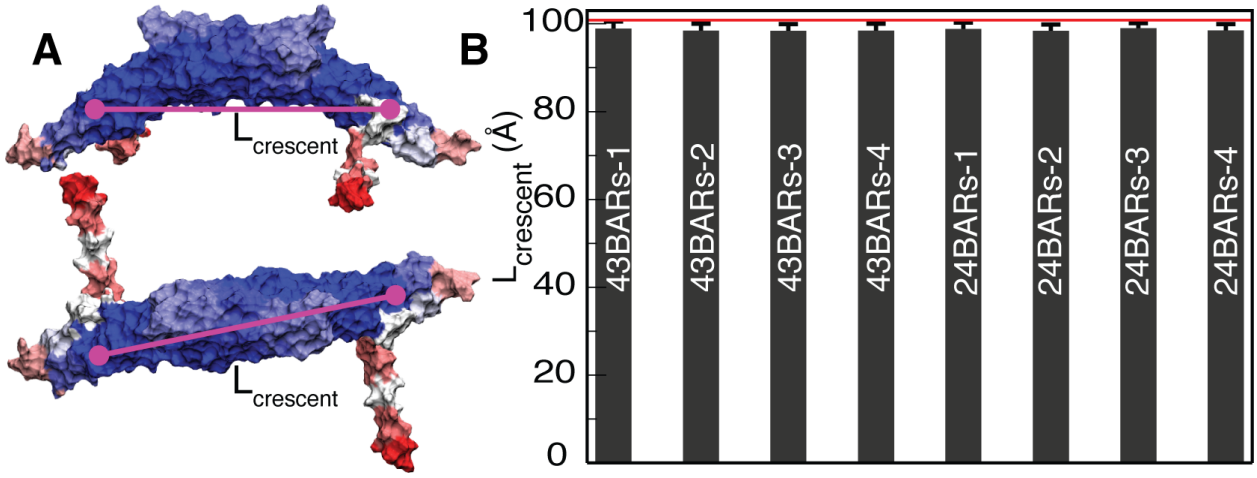

Figure S3: N-BAR domains rigidly maintain their crescent-like structure in the CG simulations. On the left panel, the N-BAR domain dimer is shown from the top and from the side, colored according to the deviation of CG beads from their positions obtained after coarse-graining the protein's crystal structure. The deviations are averaged over time, over all N-BAR domains, and over all simulations in the 24BARs and 43BARs simulation series (see Table 1 in the main text). The structure depicted is an all-atom one, where each atom is colored according to the deviation experienced by the CG bead that an atom belongs to. The color scale is linear, from deep blue (deviation of 2 Å) to deep red (deviation of 20 Å). On the right panel, the opening size, $L_{crescent}$, of the crescent-like N-BAR domain dimer is shown computed for each simulation in the 24BARs and 43BARs series. $L_{crescent}$ is averaged over time and over all N-BAR domains; error bars show the standard deviation. The horizontal red line denotes the value of $L_{crescent}$ in the crystal structure.

Fig. S3 demonstrates that the crescent-shape of the N-BAR domain dimer is maintained in the simulations (this had been already noticed during the initial parameterization of the

CG models (Arkhipov et al., 2008)). The part of the protein that comprises the main body of the crescent, with positively charged residues interacting with lipid heads, features very little deviation in its structure (blue in Fig. S3A). The crescent opening size, $L_{crescent}$, is essentially constant in all simulations, with deviations of only $\sim$2 %. On the other hand, the tips and especially the N-terminal helices are quite flexible (white and red in Fig. S3A). They feature deviations of up to 20 Å, compared to only 2 Å for the main body. Therefore, the tip-to-tip distance (data not shown) exhibits much larger deviations than $L_{crescent}$. One should note that this behavior is observed in CG simulations that are parameterized based on a 25 ns-long all-atom simulation of one N-BAR domain dimer (Arkhipov et al., 2008). Thus, the protein flexibility observed in CG simulations represents only the properties of low-amplitude vibrations of the protein structure around the starting conformation (crystal structure), while in reality the protein may undergo more dramatic fluctuations over times as long as 100 μs sampled in our CG simulations. However, it is notable that even for the CG model that describes the protein shape and flexibility in the vicinity of the crystal structure only, we observe significant differences in flexibility of different parts of the dimer. The mobility of tips and N-terminal helices are important for forming a lattice, which promotes the formation of global curvature, and for anchoring proteins to the membrane (Peter et al., 2004).

Effect of lattice type on the produced membrane curvature

To study how induced curvature depends on lattice type, we simulated a relatively small membrane patch ($64\times16\,\mathrm{nm}^2 \approx 1{,}000\,\mathrm{nm}^2$) with various arrangements of N-BAR domains (Fig. 1 of the main text). The smaller patch is chosen, instead of the larger one used for the complete tubulation simulations (Fig. 3 of the main text), because otherwise the simulations would have become prohibitively expensive computation-wise. The effect of various lattices on the global curvature becomes obvious in simulations of the smaller patch over the time of only a few microseconds (vs. $\sim$100 μs for complete tubulation), making the complete tubulation simulations (such as those in Fig. 3) unnecessary for probing this effect.

Investigation of the lattice types provided in the main text is extended in Fig. S4 through further examples. Overall, we studied 24 different lattice types (see Table 1 in the main text), twelve of which are shown in Fig. 1 of the main text, and six in Fig. S4. The six lattices not shown are very similar to those shown in Fig. 1, with only a slight difference in lateral alignment of neighboring N-BAR domain rows. The curvatures produced in simulations with these lattices are very close to curvatures shown in Fig. 1 for similar lattices. Results from all simulations taken together support the conclusion that the highest curvature is produced by lattices with between 10 and 20 N-BAR domain dimers per 1,000 nm^2, S=3-6 nm, θ=0-5°, and end-to-shoulder or end-to-end connections. It appears that the induced membrane curvature is more sensitive to the density and connection mode of dimers within the lattice than to the value of θ: while most of the lattices that produced high curvature featured θ=0-5°, one of them (see Fig. 1) had θ=20° and produced quite a high curvature, too. It should be noted that S is not an independent variable; it is determined by the choice of density, value of θ, and mode of connection. We quote the values of S here and in the main

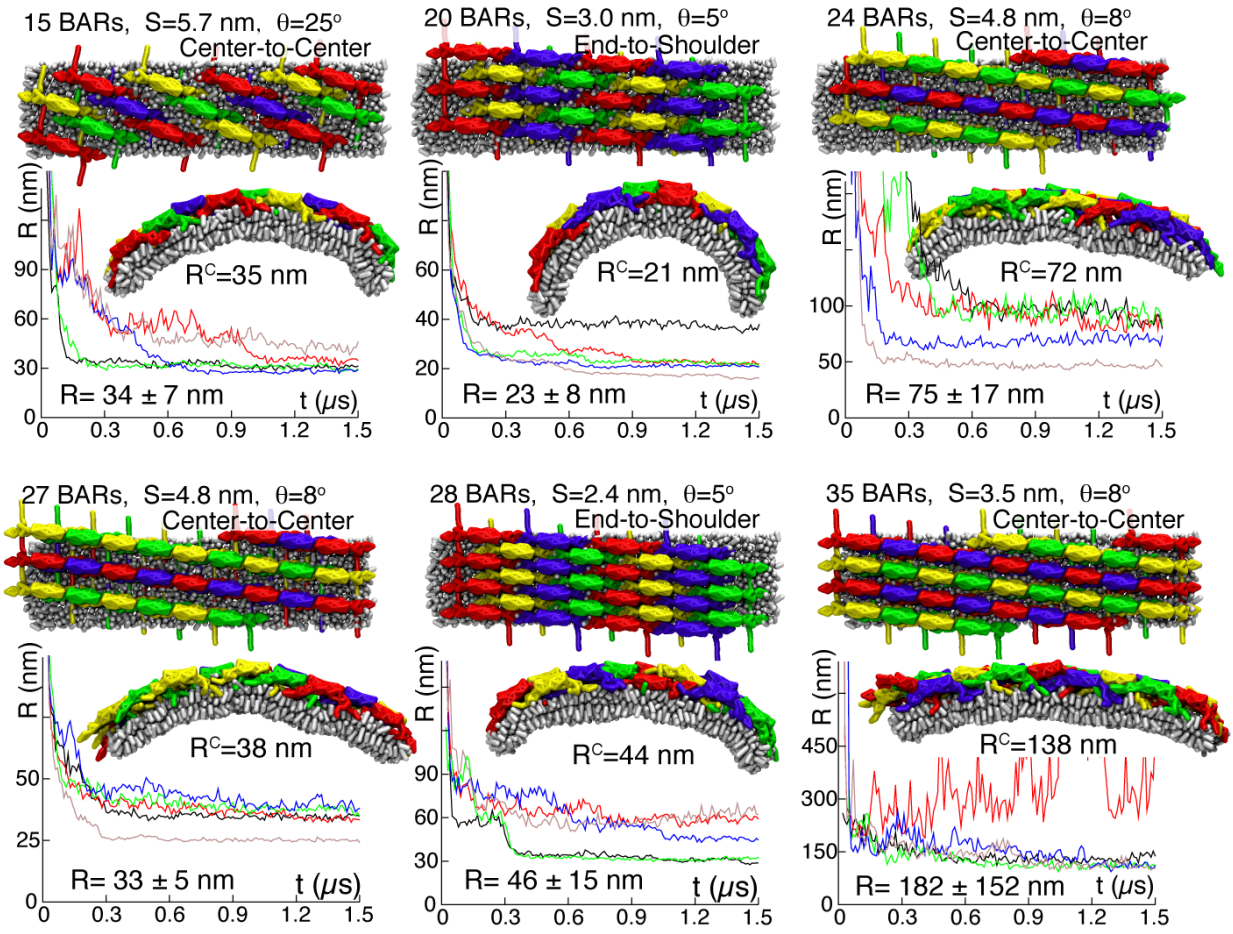

Figure S4: Membrane curvatures produced by various lattices of N-BAR domains. Lattices shown are in addition to those in Fig. 1 (all notations are the same as in the main text).

text because it can be obtained more easily from cryo-EM images (Takei et al., 1999; Peter et al., 2004; Frost et al., 2008) than other quantities, if the image resolution is low.

Inhibition of membrane bending in the case of dense lattices

Our simulations show that for N-BAR domain densities higher than ∼20 dimers per 1,000 nm^2 the membrane curvature is relatively low. Two possible reasons for this behavior were investigated. The first possibility considered is that as the lattices become denser, the neighboring rows of N-BAR domains are situated closer to each other, so that at a sufficiently high density strong contacts between rows form, rendering the whole lattice stiff. Such contacts would favor the initial flat arrangement of N-BAR domains, and it may cost a lot of energy to break the stated contacts if a bending mode is to form. However, analysis of interactions revealed that this is not the case. We considered interactions (total or electrostatic only) between N-BAR domains in the same rows and in neighboring rows, and between proteins

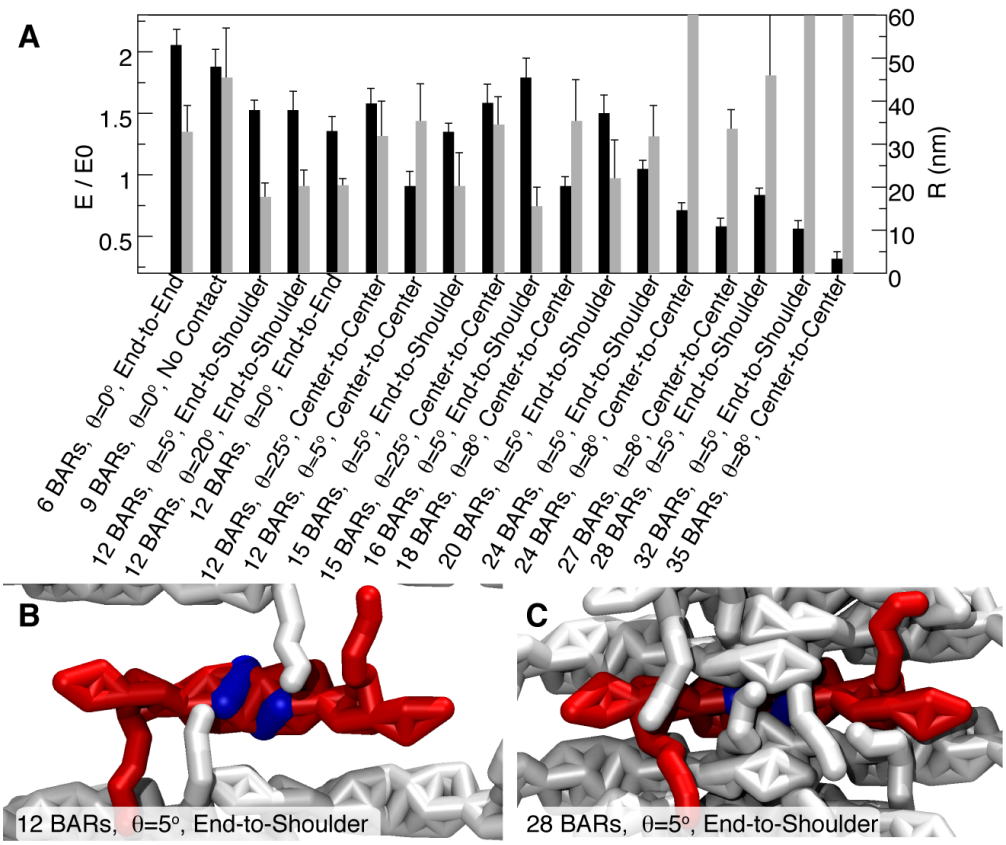

Figure S5: Occlusion of membrane-protein interaction in dense N-BAR lattices. A, Radius R (gray bars) of membrane curvature and energy E (black bars) of electrostatic interaction between the membrane and the center of the N-BAR domain's concave surface (charged part shown in blue in panels B and C). Values of E are divided by E_0, which is the value of E at $t = 0$. B, C, examples of lattices that produce high and low membrane curvatures. One N-BAR domain from the lattice is depicted (red) together with its nearest lateral neighbors (white). The view is from the membrane upwards.

and the membrane, and did not find significant differences for these energies (either total or per one dimer), or their ratios, in simulations with dense vs. sparse lattices. The second possibility considered is that the concave surface of the protein becomes separated from the membrane by the tips and N-terminal helices of neighboring proteins in the case of a dense lattice. Indeed, this hypothesis was confirmed by the analysis of corresponding interactions, as shown in Fig. S5.

Fig. S5 shows the membrane curvature in terms of radius R, which correspond to those in Fig. 1 of the main text, and the energy E of electrostatic interaction between the membrane and the center of the N-BAR domain's concave surface. The values of E are given per one N-BAR domain dimer; they are averaged over time and over all simulations for each type of lattice, and divided by E_0, which is the value of E at $t = 0$ (after minimization), averaged

over all lattices (values of E_0 for different lattices are the same within 10 %). For lattices with $>$ 20 N-BAR domain dimers per 1,000 nm^2, E/E_0 is low, demonstrating that the protein's concave surface is out of contact with the membrane.

Fig. S5B,C shows examples of a lattice with an "optimal" density (12 BARs), as well as a high-density one (28 BARs), producing $R = 17$ nm and $R = 46$ nm, respectively. For the 12 BARs lattice, the contact between the N-BAR domain concave surface and the membrane is free to form, resulting in efficient scaffolding. For a dense lattice such as 28 BARs, this contact for each N-BAR domain is occluded by many N-terminal helices and tips from neighboring N-BAR domains, which cover the membrane surface. This occlusion is the reason why the scaffolding is not proceeding efficiently for dense lattices (or, in other words, E/E_0 in Fig. S5A is low).

The values of E/E_0 are 1.1±0.3 and 2.0±0.2 for the all-atom simulation 8BARs-AA and the analogous CG simulation 8BARs-CG, respectively. For the latter, this value is close to $E/E_0 = 1.8 \pm 0.1$ that is obtained in CG simulations with 16 N-BARs per 1,000 nm^2 for a similar lattice type, but on a twice wider membrane patch (see 16 BARs lattice in Figs. 1B of the main text and S5A). The smaller value of E/E_0 for 8BARs-AA is probably due to the fact that, on the available time scale, membrane bending is still in progress, i.e., full contact between the N-BAR domains and the membrane has not been established yet. On the other hand, the value of E/E_0 in the 8BARs-AA case is higher than that for the dense N-BAR domain lattices, as found in the CG simulations (Fig. S5A), suggesting that the 8BARs-AA lattice should bend the membrane well, which is indeed observed for both all-atom and CG simulations (Fig. 2 of the main text). Interestingly, the initial electrostatic interaction energy between the membrane and the center of N-BAR domain's concave surface are the same for 8BARs-AA and 8BARs-CG (107.5 vs. 108.1 kcal/mol per one N-BAR domain), even though the CG model was not tuned to reproduce actual interaction energies, adding to the evidence that a choice of $\varepsilon = 1$ in the SBCG model is sensible (see EXPERIMENTAL PROCEDURES in the main text).

Elastic bending energy of the membrane

The elastic bending energy of the membrane is calculated using the Helfrich elastic membrane theory (Helfrich, 1973), according to which the bending energy can be computed as

$$E_{bend}^{tot} = \frac{k_c A}{2R^2}, \tag{2}$$

where k_c is the bending rigidity (for our CG model, $k_c \approx 20 k_B T$, k_B being the Boltzmann constant and $T = 300$ K the temperature, as estimated in Arkhipov et al. (2008)), A is the membrane area and R the curvature radius. Uniform one-dimensional curvature is assumed, in agreement with the fact that in our simulations bending develops along the long dimension of the membrane patch, while along the short dimension no detectable curvature is observed. The energy E_{bend}^{tot} is divided by the number of N-BAR domain dimers in each lattice to obtain

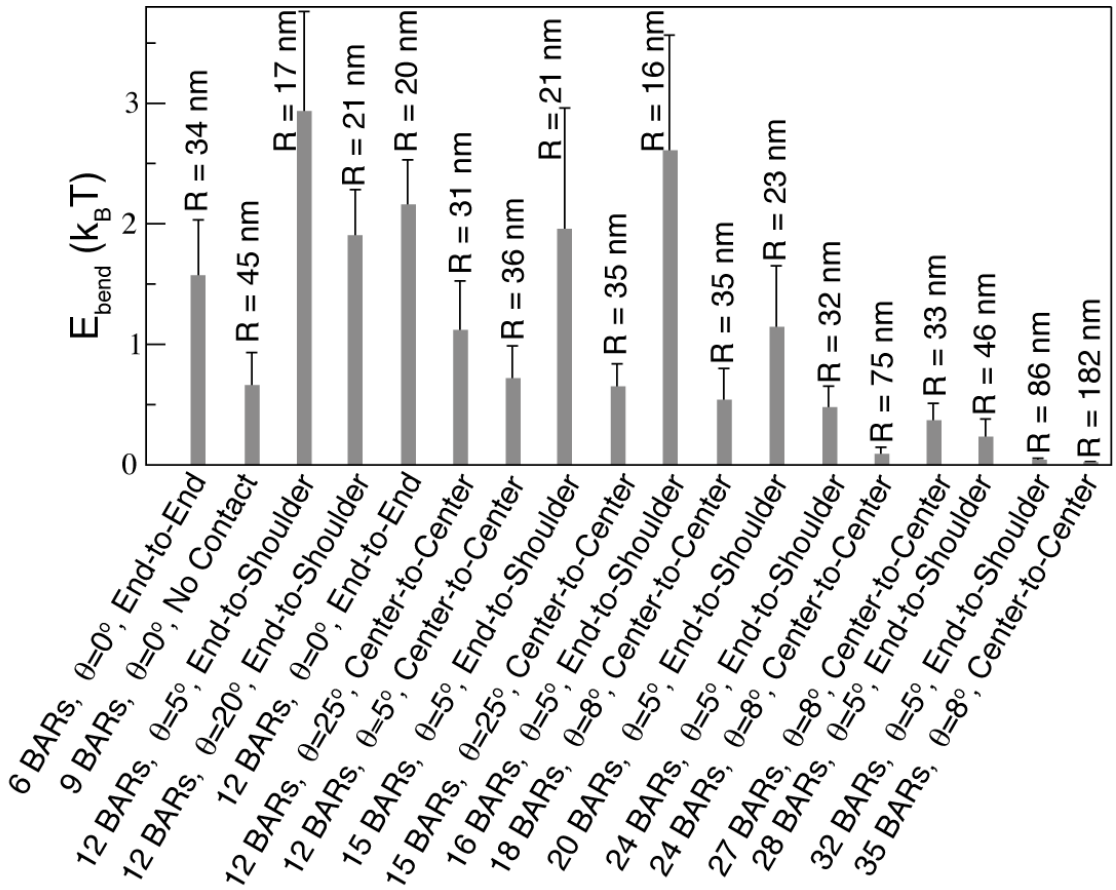

Figure S6: Membrane bending energy E_{bend} per N-BAR domain dimer. E_{bend} is given in units of k_BT, assuming $T = 300\,\mathrm{K}$. Error bars represent standard deviation of E_{bend} due to the averaging over five simulations for each lattice (see simulations BAR-lattices in Table 1 of the main text; the membrane patch area is the same in all these simulations). Average membrane bending radii R observed for each lattice are indicated near respective data points.

E_{bend} plotted in Fig. S6, providing the contribution of a single dimer on membrane bending. Data in Fig. S6 confirm once again that the density of N-BAR domains in a lattice is not the only defining factor for the amount of curvature established. The orientation of N-BAR domains and contacts between them within the lattice, along with the density, determine the amount of bending, and the bending energy E_{bend} per one N-BAR domain dimer can be very different for lattices of the same density. However, for all lattices with significant curvature ($R < 30\,\mathrm{nm}$), values of E_{bend} are 1-3 k_BT, which is noticeably higher than E_{bend} for lattices with shallow curvature. As Fig. S5 shows, when a lattice is too dense or protein-protein contacts are not optimal, interactions between N-BAR domains and the membrane that promote bending can be occluded. This reduces the amount of energy that one N-BAR domain can apply to bend the membrane (c.f. Figs. S5 and S6).

Previous all-atom and CG simulations (Blood and Voth, 2006; Blood et al., 2008; Arkhipov et al., 2008) showed that a single N-BAR domain on a membrane patch can produce membrane curvature with $R = 10 - 50\,\mathrm{nm}$, the value strongly fluctuating between independent simulations and within a single simulation; the R value is established locally, i.e., not globally as in the case of lattices considered here. The length of a single N-BAR domain is 15 nm, and the width of the membrane patch simulated in Arkhipov et al. (2008) is 10 nm. Thus, one estimates the membrane area affected by local bending to be $A = 15 \times 10\,\mathrm{nm}^2 = 150\,\mathrm{nm}^2$. Using Eq. 2 for membrane bending by a single N-BAR domain, one then estimates $E_{bend} = 0.6$ - $15\,k_BT$, i.e., a highly fluctuating value. **Applying Eq. 2 to the results of the all-atom simulation 8BARs-AA, we find $E_{bend} = 0.15\,k_BT$, but this low value is due to the incomplete curvature of the membrane, as the bending is still ongoing in this simulation. For 8BARs-CG, we find $E_{bend} = 1.6 \pm 0.2\,k_BT$, which is close to the value of $2.6 \pm 0.9\,k_BT$ that we determine for the similar 16 BARs per 1,000 nm^2 lattice (Fig. S6). In CG simulations,** for lattices producing high curvature one finds $E_{bend} = 1 - 3\,k_BT$. We conclude that strong membrane bending in the case of "optimal" lattices requires only a moderate bending energy input from each N-BAR domain.

References

Arkhipov, A., Freddolino, P.L., Imada, K., Namba, K., and Schulten, K. (2006a). Coarse-grained molecular dynamics simulations of a rotating bacterial flagellum. Biophys. J. *91*, 4589–4597.

Arkhipov, A., Freddolino, P.L., and Schulten, K. (2006b). Stability and dynamics of virus capsids described by coarse-grained modeling. Structure *14*, 1767–1777.

Arkhipov, A., Yin, Y., and Schulten, K. (2008). Four-scale description of membrane sculpting by BAR domains. Biophys. J. *95*, 2806–2821.

Blood, P.D., Swenson, R.D., and Voth, G.A. (2008). Factors influencing local membrane curvature induction by N-BAR domains as revealed by molecular dynamics simulations. Biophys. J. *95*, 1866–1876.

Blood, P.D., and Voth, G.A. (2006). Direct observation of Bin/amphiphysin/Rvs (BAR) domain-induced membrane curvature by means of molecular dynamics simulations. Proc. Natl. Acad. Sci. USA *103*, 15068–15072.

Feller, S.E. (2000). Molecular dynamics simulations of lipid bilayers. Curr. Opin. Coll. & Interf. Sci. *5*, 217–223.

Freddolino, P.L., Arkhipov, A., Shih, A.Y., Yin, Y., Chen, Z., and Schulten, K. (2008). Application of residue-based and shape-based coarse graining to biomolecular simulations. In G. A. Voth, editor, *Coarse-Graining of Condensed Phase and Biomolecular Systems*, chapter 20. Chapman and Hall/CRC Press, Taylor and Francis Group, 299–315.

Frost, A., Perera, R., Roux, A., Spasov, K., Destaing, O., Egelman, E.H., De Camilli, P., and Unger, V.M. (2008). Structural basis of membrane invagination by F-BAR domains. Cell *132*, 807–817.

Helfrich, W. (1973). Elastic properties of lipid bilayers: theory and possible experiments. Z. Naturforsch. *28*, 693–703.

Humphrey, W., Dalke, A., and Schulten, K. (1996). VMD – Visual Molecular Dynamics. J. Mol. Graphics *14*, 33–38.

Isralewitz, B., Gao, M., and Schulten, K. (2001). Steered molecular dynamics and mechanical functions of proteins. Curr. Opin. Struct. Biol. *11*, 224–230.

Jorgensen, W.L., Chandrasekhar, J., Madura, J.D., Impey, R.W., and Klein, M.L. (1983). Comparison of simple potential functions for simulating liquid water. J. Chem. Phys. *79*, 926–935.

MacKerell, A., Jr., Bashford, D., Bellott, M., Dunbrack, R.L., Jr., Evanseck, J., Field, M.J., Fischer, S., Gao, J., Guo, H., Ha, S., et al. (1998). All-atom empirical potential for molecular modeling and dynamics studies of proteins. J. Phys. Chem. B *102*, 3586–3616.

Peter, B.J., Kent, H.M., Mills, I.G., Vallis, Y., Butler, P.J.G., Evans, P.R., and McMahon, H.T. (2004). BAR domains as sensors of membrane curvature: The amphiphysin BAR structure. Science *303*, 495–499.

Phillips, J.C., Braun, R., Wang, W., Gumbart, J., Tajkhorshid, E., Villa, E., Chipot, C., Skeel, R.D., Kale, L., and Schulten, K. (2005). Scalable molecular dynamics with NAMD. J. Comp. Chem. *26*, 1781–1802.

Takei, K., Slepnev, V.I., Haucke, V., and De Camilli, P. (1999). Functional partnership between amphiphysin and dynamin in clathrin-mediated endocytosis. Nat. Cell Biol. *1*, 33–39.